Available online at www.sciencedirect.com
SCIENCE DIRECT®
ELSEVIER
Earth and Planetary Science Letters 214 (2003) 645–654
EPSL
www.elsevier.com/locate/epsl

Elasticity and strength of hydrous ringwoodite at high pressure

Abby Kavner *

Lamont Doherty Earth Observatory, 61 Rt. 9W, Palisades, NY 10964, USA

Received 18 March 2003; received in revised form 27 June 2003; accepted 10 July 2003

Abstract

OH^--bearing (hydrous) ringwoodite compressed non-hydrostatically in a diamond anvil cell supports a differential stress that increases from 2.9 to 4.5 GPa over the pressure range of 6.7–13.2 GPa at room temperature. This result suggests a significant water weakening effect when compared with results from similar experiments on the anhydrous counterpart [Kaver and Duffy, Geophys. Res. Lett. 28 (2001) 2691–2694]. The elastic anisotropy ($=2C_{44}/(C_{11}-C_{12})$ of hydrous ringwoodite is measured to be 0.87(7) throughout this pressure range, similar to measured values for anhydrous ringwoodite [Kaver and Duffy, Geophys. Res. Lett. 28 (2001) 2691–2694]. This lattice anisotropy cannot be explained by anelastic effects such as faulting and twinning within the structure. These results suggest that hydrous minerals in the upper mantle and transition zone may have higher ductile strain rates for a fixed shear stress at high temperature, resulting in stronger preferred lattice orientation. This, in turn, may be seismically detectable, which opens the possibility of using seismic anisotropy as a marker for local volatile-containing areas within the upper mantle and transition zone.

Keywords: high-pressure; deformation; transition zone; hydrous minerals; anisotropy

1. Introduction

Most nominally anhydrous minerals are able to store moderate amounts (tens to hundreds of ppm) of water as hydroxyl (OH^-) within their structure [2]. X-ray diffraction and spectroscopic measurements have shown that the transition zone polymorphs of olivine, wadsleyite [3–6] and ringwoodite [7,8], may store comparatively large amounts of OH^- in their structures, up to a few percent. In addition to serving as a conduit for the transfer of water between the Earth's surface and its deep interior, OH^--bearing minerals may have a strong influence on mantle rheology. Small amounts of OH^- disproportionately affect the physical properties of nominally anhydrous minerals, especially by lowering melting temperature and decreasing viscosity [9]. Since the transition zone between the Earth's upper and lower mantle helps govern the scale of mass and heat transport

* Present address: Earth and Space Sciences Department and Institute for Geophysics and Planetary Physics, UCLA, Los Angeles, CA 90095, USA. Fax: +1-310-825-2779.
E-mail address: akavner@ucla.edu (A. Kavner).

0012-821X/03/$ – see front matter © 2003 Elsevier B.V. All rights reserved.
doi:10.1016/S0012-821X(03)00402-3

throughout the Earth, the presence of water within this region, whether global or localized, may have a significant effect on mantle rheology and therefore mantle circulation.

Elucidating the deep-Earth component of the volatile cycle requires tying together mineral physics measurements of how the presence of water alters the physical properties of Earth materials with seismic observations of mantle processes [10]. Recent seismic studies show that the transition zone has a measurable azimuthal elastic anisotropy [11]. The physical interpretation points to a lattice preferred orientation in transition zone minerals. Interpreting these data requires knowing the elastic moduli, including elastic anisotropy of transition zone minerals at the relevant pressures and temperatures, and how those elastic properties change with changes in pressure, temperature, and composition, including the presence of volatile phases.

Though we are all pushing toward this goal, at this point in time no mineral physics laboratory is capable of completely duplicating the conditions of the Earth's interior – including the ability to subject the proper phase assemblages to the appropriate pressures, temperatures, and strain rate. Therefore, our understanding of mantle minerals is based on combining information from a pastiche of experiments performed at a variety of conditions, to look for trends in behavior that can be extrapolated to the deep-Earth conditions. Here, the goal is to understand how the addition of hydroxyl changes the rheology and elastic properties of ringwoodite, perhaps one of the dominant transition zone minerals. To this end, synchrotron-based powder X-ray diffraction techniques were used to examine the behavior of hydrous ringwoodite under extreme non-hydrostatic conditions in the diamond anvil cell to see how the addition of OH^- within a transition zone mineral's structure affects its rheology, including elastic properties, especially elastic anisotropy, and resistance to shear deformation.

2. Experimental methods

Polycrystalline hydrous ringwoodite was synthesized at 1400°C and 20 GPa in the 5000-ton multi-anvil press at the Bayerisches Geoinstitut in Germany by J. Smyth of the University of Colorado. The crystals contain about 2.2 wt% H_2O and have a composition of $Mg_{1.63}Fe_{0.22}H_{0.4}Si_{0.95}O_4$, with $\sim$10% ferric iron, based on electron microprobe analysis, infrared spectroscopy, and Mossbauer spectroscopy [8]. The room pressure unit cell parameter determined by refinement from the centering angles of 20 reflections is 8.093(2) Å. Impurities of wadsleyite, stishovite, and/or quenched glass might be present within the sample [8]. Hydrous ringwoodite powder was loaded inside a 100 μm sample chamber within a beryllium gasket inside a diamond anvil cell equipped with 350 μm culets. Several small chips of ruby were placed across the surface of the sample as a fluorescence pressure calibrant.

Radial X-ray diffraction experiments were performed at beamline X17C of the National Synchrotron Light Source, using white radiation and a multi-channel solid state detector, using the same procedure as in [1]. The size of the incident X-ray beam was 10 μm × 15 μm. The diamond cell was positioned for radial diffraction such that the X-ray beam passed between the two diamond faces, through the beryllium gasket and the sample. Energy-dispersive diffraction patterns were collected at a fixed Bragg angle of $2\theta = 12.000(3)°$ for 15–45 min. At each loading step of the diamond cell, a pressure was measured via ruby fluorescence at five or more places across the width of the sample chamber. The average value and standard deviation were calculated and used as the nominal indicator of the average hydrostatic pressure in the sample chamber. Given that the sample chamber was under non-hydrostatic stress at all compressions, the significance of this 'pressure' determination is discussed in the following sections. At each of the seven pressure steps, 5–15 diffraction patterns were obtained at different angles relative to the principal stress direction by rotating the diamond anvil cell about the axis defined by the incoming X-ray beam. Further details of these experiments and analysis are given elsewhere [1,12–15].

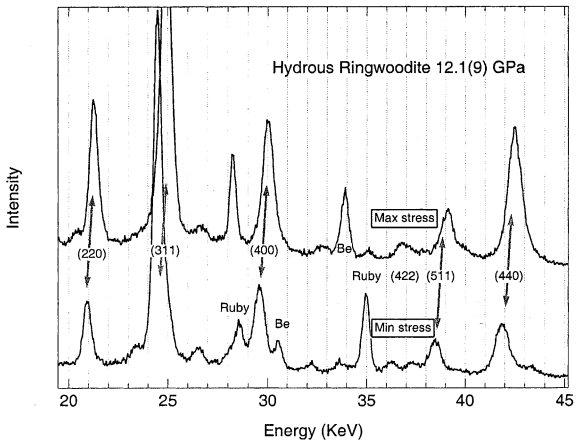

Fig. 1. X-ray diffraction patterns under maximum stress ($\psi=0°$) and minimum stress ($\psi=90°$) conditions ($2\theta=12.000(3)$). Hydrous ringwoodite diffraction peaks are indexed with their (hkl) values, with gray arrows indicating peaks used in the analysis. Diffraction peaks arising from ruby and Be are indicated.

3. Analysis

Samples within a non-hydrostatically loaded diamond cell are subjected to a biaxial stress state, where the maximum principal stress, σ_1, is perpendicular to the diamond faces and greater than the minimum principal stress, σ_3, provided by the gasketting material (and/or friction against the diamonds) in the radial direction. The differential stress, $t=\sigma_1-\sigma_3$, elastically supported by a polycrystalline cubic material within a diamond anvil cell can be calculated using finite strain theory assuming cylindrical symmetry in the sample chamber and constant stress across grain boundaries (Reuss condition) through the equation [13]:

$$\varepsilon(\psi,hkl)-\varepsilon_{\mathrm{hydro}} = (t/3)(S_{11}-S_{12}-3S\Gamma(hkl))(1-3\cos^2\psi) \quad (1)$$

where $\varepsilon(\psi,hkl)$ is the total lattice strain measured by X-ray diffraction, which varies as a function of both the Miller indices of the reflecting plane (hkl), and the angle between the diffracting plane normal and the maximum principal stress (ψ); $\varepsilon_{\mathrm{hydro}}$ is the hydrostatic component of the strain; the S_{ij}s are single crystal elastic compliances; S is a measure of the elastic anisotropy, equal to $S_{11}-S_{12}-0.5S_{44}$; and Γ is an orientation factor given by $(h^2k^2+k^2l^2+h^2l^2)/(h^2+k^2+l^2)^2$. According to Eq. 1, at $\psi=54.7°$, the measured lattice strain is not a function of (hkl), and is equal to the hydrostatic component of the strain, $\varepsilon_{\mathrm{hydro}}=(2\varepsilon_{90}+\varepsilon_0)/3$.

Under Voigt conditions (constant strain), the lattice strain is not a function of (hkl), and is equal to:

$$\langle\varepsilon_{(hkl)}\rangle-\varepsilon_{\mathrm{hydro}} = (t/3)(1/G_{\mathrm{v}})(1-3\cos^2\psi) \quad (2)$$

where G_{v} is the Voigt shear modulus. The Voigt strain falls between the two strain endmembers determined by the lattice planes corresponding to the maximum and minimum Γ values via Eq. 1.

In an elastically isotropic material, each of the lattice planes shows the same strain, and the Voigt and Reuss strains become identical.

For each of the 63 diffraction patterns, diffraction peaks corresponding to hydrous ringwoodite, ruby, and the beryllium gasket were identified (Fig. 1). The observation of some small extra peaks in some of the diffraction patterns can be attributed to the presence of minor impurities within the hydrous ringwoodite. The largest of these peaks, at 28 keV (d-spacing of 2.118 Å) is shown in one of the diffraction patterns in Fig. 1. Since it only appears at that one pressure in that single orientation, it presumably arises from a small, highly oriented single crystal. In each diffraction pattern, the best-fit center energy of each of the five strongest hydrous ringwoodite diffraction peaks, (220), (311), (400), (511), and (440), was determined. For each of these energies, d-spacing (Table 1), lattice parameter, and Eulerian strains (referenced to $a_0=8.093(2)$ Å) were calculated as a function of (hkl), angle, and pressure. Diffraction peaks shift by 1–2% to higher energy (lower d-spacing) as the angle is changed from minimum to maximum stress conditions (Fig. 1 and Table 1). This shift is significant; for example, the (220) peak shifts from a center energy of 21.274 keV (2.788 Å) to 20.940 keV (2.832 Å): a difference of 33.4 eV (0.044 Å) between maximum and minimum stress direction. By com-

Table 1
All d-spacings for hydrous ringwoodite diffraction peak fits

Name	220	311	400	511	440	Angle
rwp1_001	2.8458	2.4256	2.0159	1.5481	1.4236	90
rwp1_002	2.8349	2.4217	2.0063	1.5436	1.4202	180
rwp1_003	2.8404	2.4227	2.0152	1.5497	1.4205	160
rwp1_004	2.8363	2.4217	2.0056	1.5445	1.4192	140
rwp1_005	2.8458	2.4247	2.0125	1.5497	1.4256	90
rwp2_001	2.8417	2.4276	2.0104		1.4212	90
rwp2_002	2.8417	2.4207	2.0111			80
rwp2_003	2.8282	2.4109	1.9982	1.5388	1.4158	50
rwp2_004	2.8134	2.3992	1.9895	1.5321	1.4084	30
rwp2_005	2.8001	2.3982	1.9902			10
rwp2_006	2.8121	2.3924	1.9888		1.4070	180
rwp2_007	2.8094	2.4040	1.9942		1.4054	200
rwp2_008	2.8094	2.4011	1.9888	1.5285	1.4064	160
rwp2_009	2.8215	2.4118	1.9962	1.5420		140
rwp2_010	2.8363	2.4187	2.0070			120
rwp2_011	2.8404	2.4256	2.0090	1.5481	1.4215	100
rwp3_001	2.7955	2.3895	1.9824	1.5233	1.4001	180
rwp3_002	2.8310	2.4177	2.0048	1.5443	1.4154	90
rwp3_003	2.8310	2.4201	2.0048			70
rwp3_004	2.8363	2.4220	2.0087	1.5443	1.4185	110
rwp3_005	2.8173	2.4100	1.9886	1.5334	1.4106	130
rwp3_006	2.8037	2.3896	1.9817	1.5280	1.4031	150
rwp3_007	2.7957	2.3864	1.9781	1.5232	1.4002	170
rwp3_008	2.7954	2.3942	1.9832	1.5300	1.4031	200
rwp4_001	2.8294	2.4149	2.0019	1.5435	1.4162	90
rwp4_002	2.8389	2.4152	1.9986	1.5414	1.4150	100
rwp4_003	2.8316	2.4122	2.0027	1.5404	1.4164	110
rwp4_004	2.8146	2.4116	1.9922		1.4082	120
rwp4_005	2.8146	2.3988	1.9902		1.4074	130
rwp4_006	2.8025	2.3904	1.9807	1.5261	1.4021	140
rwp4_007	2.8007	2.3905	1.9814	1.5238	1.4021	150
rwp4_008	2.7941	2.3851	1.9775		1.3992	160
rwp4_009	2.7909	2.3815	1.9757	1.5209	1.3968	170
rwp4_010	2.7896	2.3866	1.9785	1.5206	1.3974	180
rwp4_011	2.8339	2.4195	2.0072	1.5457	1.3849	90
rwp4_012		2.4195				80
rwp4_013	2.7903	2.3886	1.9775	1.5227	1.3971	10
rwp4_014	2.7983	2.3901	1.9795	1.5254	1.4005	20
rwp4_015	2.8050	2.3957	1.9846	1.5303	1.4036	30
rwp5_001	2.7876	2.3815	1.9757	1.5174	1.3951	180
rwp5_002	2.7886	2.3821	1.9768	1.5227	1.3964	160
rwp5_003	2.8015	2.3971	1.9839	1.5247	1.4024	140
rwp5_004	2.8149	2.4033	1.9927	1.5337	1.4083	120
rwp5_005	2.8318	2.4211	2.0056	1.5425	1.4163	90
rwp5_006	2.7849	2.3801	1.9726	1.5187	1.3946	160
rwp5_007	2.7997	2.3924	1.9815	1.5253	1.4022	140
rwp5_008	2.8153	2.4031	1.9922	1.5318	1.4088	120
rwp5_009	2.8309	2.4088	2.0050	1.5378	1.4161	90
rwp5_010	2.8283	2.4113	1.9949	1.5400	1.4150	70
rwp6_002	2.7849	2.3806	1.9708	1.5145	1.3936	150
rwp6_003	2.8061	2.3960	1.9838	1.5266	1.4066	130
rwp6_004	2.8231	2.4071	1.9923	1.5380	1.4113	110
rwp6_005	2.8259	2.3985	2.0019	1.5353	1.4132	90

Table 1 (*Continued*).

Name	220	311	400	511	440	Angle
rwp6_007	2.8268	2.4119	2.0008	1.5391	1.4139	90
rwp6_008	2.8268	2.4122			1.4110	70
rwp6_009	2.8205	2.4048	1.9940	1.5339	1.4107	110
rwp6_010	2.7942	2.3804	1.9753	1.5211	1.3989	40
rwp6_011	2.7773	2.3728	1.9678	1.5119	1.3904	20
rwp6_012	2.7746	2.3711	1.9668	1.5121	1.3885	0
rwp6_013	2.7829	2.3809	1.9742			20
rwp7_002	2.8160	2.4030	1.9915	1.5349	1.4087	110
rwp7_005	2.8197	2.4069	1.9888	1.5353	1.4100	70
rwp7_006	2.8198	2.4128	1.9992	1.5372	1.4095	90

parison, the center position of each peak is fit to a precision of 2–4 eV (0.0002–0.0005 Å). The shifts correspond to an effective pressure difference of ~9–10 GPa with peak precisions of ~0.1 GPa, if lattice strains are referred to a ringwoodite P(V) equation of state. Except for the final pressure step, the relative X-ray peak intensities remained close to those expected for a randomly oriented powder, indicating no strain-induced preferred orientation. Throughout the experiment, and especially in the final two pressure steps, there was a gradual loss of overall X-ray intensity around the maximum stress direction ($0° \pm \sim 50°$), thereby precluding a strength analysis for the highest pressure run. Even during these last pressure steps, the relative peak intensities of ringwoodite remained the same; therefore this loss in intensity cannot be easily attributed to a texturing effect.

At each pressure step, the positions of the five diffraction peaks are fit as a linear function of $1-3\cos^2\psi$, providing two parameters for each (*hkl*) (Fig. 2). (i) The *y*-intercept, defined by $1-3\cos^2\psi = 0$, gives the hydrostatic lattice parameter. (ii) The slope of the ψ-dependent lattice response represents a product of t, the supported differential stress, and a combination of the elastic constants, given by Eq. 1. At a given pressure step, all of the separate (*hkl*) fits can be used together to measure the sample's anisotropic response. The anisotropy signal was determined by plotting the slopes determined in (ii) as a function of Γ, which in this experiment ranges from 0 for the (400) line to a maximum of 0.25 for the (220) and (440) lines (Fig. 3a). If this line shows a positive slope, its elastic anisotropy is <1; a negative slope indicates the elastic anisotropy is >1. Under Reuss (constant stress) conditions, the magnitude of the elastic anisotropy can be determined by taking the ratio of Eq. 1 determined for both $\Gamma_{\min}$ ($=0$) and $\Gamma_{\max}$ ($=1/3$):

$$= (t/3)(S_{11}-S_{12}-3S\Gamma_{\min})(1-3\cos^2\psi)/$$
$$(t/3)(S_{11}-S_{12}-3S\Gamma_{\max})(1-3\cos^2\psi)$$
$$= (S_{11}-S_{12})/0.5(S_{44}) = 2C_{44}/(C_{11}-C_{12}) \quad (3)$$

This assumes that anelastic contributions to lattice strain anisotropy can be ignored, as discussed in more detail in Section 4.2. This provides a lower bound to the absolute value of the anisotropy; any contribution from constant-strain conditions will serve to dampen the anisotropy signal. Note that this anisotropy measurement is independent of both pressure and supported differential stress. However, the anisotropy signal becomes clearer if the sample supports a larger differential stress. In this analysis, constant stress (Reuss) condition is assumed. In Section 4.2, the effects of the possibility of conditions intermediate between constant stress and constant strain (Voigt–Reuss bounds) are explored.

4. Results and discussion

4.1. Strength

A simple model describing material strength claims a material can support a deviatoric stress

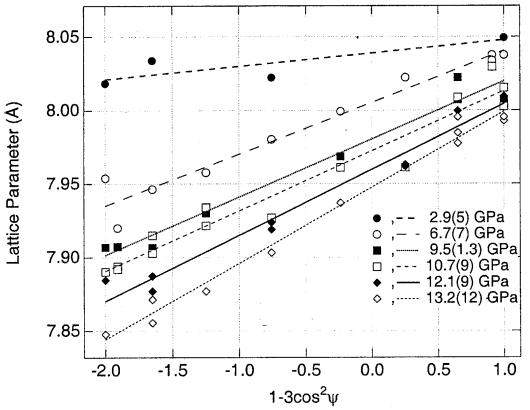

Fig. 2. Lattice parameter vs. $1-3\cos^2\psi$ for (220) diffraction line of hydrous ringwoodite for each data set. Pressure is determined by ruby fluorescence. Linear fits are shown through each of the data sets.

up to its elastic limit, after which the material yields plastically [16]. Therefore differential stress, as measured here, provides a lower bound to the material's yield strength. In these experiments, the differential stress can be approximated by considering an average of all of the (*hkl*) responses at a single compression via $t = 6G^{\mathrm{Reuss}}\langle(\varepsilon_{\mathrm{hydro}}-\varepsilon_{90})\rangle$ [13]. The shear modulus of hydrous ringwoodite, $G_0^{\mathrm{Reuss}} = 107(3)$ [17] was extrapolated to high pressures using a Birch equation of state [18], assuming $\mathrm{d}G/\mathrm{d}P = 1.5$. The range of published $\mathrm{d}G/\mathrm{d}P$ values for ringwoodite (both hydrous and anhydrous) spans from 1.2 to 1.8 [17,19,20]. The resulting high pressure variance of G propagates into an error of less than 5% in the strength calculation, well within the uncertainties. Hydrous ringwoodite supports a differential stress of 2.9–4.5 GPa over the pressure range of 6.7–13.2 GPa, a 50% decrease relative to anhydrous ringwoodite, which supports 6–8 GPa over the same pressure range (Fig. 4) [1]. Strength results in general are extremely history-dependent, and in diamond cell experiments may vary with the diamond size, gasket material and hole radius. In this case, the radial diffraction measurements were done under almost identical conditions, making the comparison between the strength of hydrous and anhydrous ringwoodite more reliable.

One of the assumptions of the lattice strain theory is that the stress tensor is spatially invariant within the diamond anvil cell sample chamber. However, under non-hydrostatic conditions, significant pressure gradients may exist there [21–24]. For example, in the highest pressure data set for which there is a reliable strength measurement (rwp6) ruby fluorescence measurements from separate ruby grains across the sample surface yielded values of 14.6, 13.8, 13.2, 12.7. and 11.5 GPa across a $\sim$40 μm radius from the center of

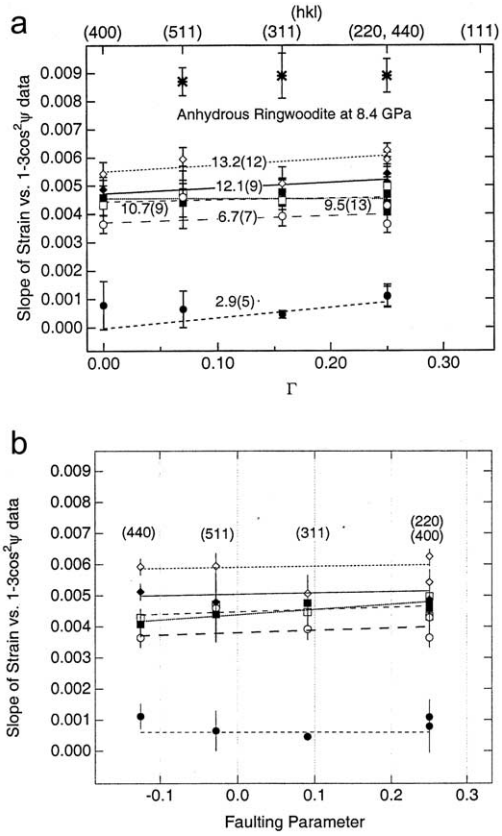

Fig. 3. (a) Anisotropy signal. The slopes of all of the (*hkl*) vs. $1-3\cos^2\psi$ fits are plotted as a function of $\Gamma(hkl)$ at each compression step. The pressures (in GPa) are labeled for each line. The results for anhydrous ringwoodite are shown as stars. Slope and χ^2 values from these straight-line fits are shown in Table 2. (b) Faulting signal. The slopes of all of the (*hkl*) vs. $1-3\cos^2\psi$ fits are plotted as a function of faulting parameter [26] at each compression step. The pressures (in GPa) are labeled for each line. Note that the order of the (*hkl*) planes on the *x*-axis is different in panel b than in panel a, due to the different *hkl* dependences of faulting and elastic anisotropy. Results from straight-line fits are shown in Table 2.

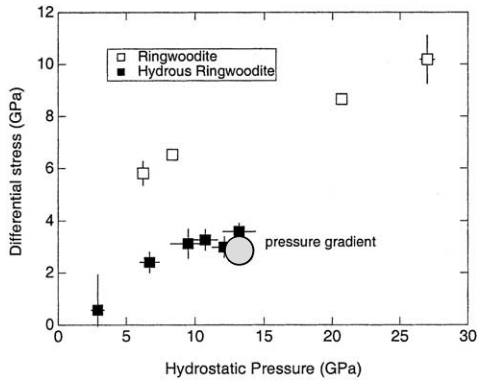

Fig. 4. Elastically supported differential stress of both hydrous and anhydrous ringwoodite [1] (open and filled squares, respectively) as a function of pressure. The hatched area shows the supported differential stress for the highest pressure run of hydrous ringwoodite determined using the pressure gradient method (see text).

the sample to the gasket edge. This suggests that the 10×15 μm X-ray beam sampled a volume of hydrous ringwoodite experiencing a pressure gradient on the order of 1 GPa. This is lower than the supported differential stress measured by lattice strain theory, and the primary manifestation of this stress gradient would be broader X-ray diffraction peaks.

An alternative method to measure the elastically supported differential stress (t) of materials at high pressures takes advantage of these pressure gradients to calculate:

$$t \approx \sigma_y = h(dP/dr) \quad (4)$$

where σ_y is the yield strength, h is the sample thickness, P is the pressure measured by ruby fluorescence, and r is the radial distance from the center of the diamond anvil cell axis [22–24]. In this experiment, the sample thickness was estimated by scanning the diamond cell through the stationary X-ray beam, yielding an estimate of 42 μm determined from the FWHM of intensity of transmitted X-ray beam plotted as a function of distance. The pressure gradient method gives an approximate measure of the differential stress inside the diamond cell to be ~3 GPa; in general agreement with the values from radial diffraction values (Fig. 4). Together, these two independent measurements, under similar high pressure, room temperature, and diamond cell strain rate conditions, demonstrate profound weakening caused by structural accommodation of OH^- in the transition zone mineral ringwoodite.

4.2. Anisotropy

The lattice anisotropy is calculated by taking the ratio of the strains determined at the Γ extrema: where $\Gamma = 0$ and 0.333, as described in Section 3. These values were extrapolated from linear fits through the data shown in Fig. 3, and plotted as a function of pressure in Fig. 5. The anisotropy has an average value of 0.87(7) in this pressure range, in agreement with previous measurements of ringwoodite using radial diffraction techniques [1]. (Note that anisotropy is plotted here as a ratio $2C_{44}/(C_{11}-C_{12})$ instead of $S_{11}-S_{12}-0.5S_{44}$ as plotted previously, and in other presentations of results from radial diffraction.) Although each of the measurements has a large error bar, the scatter in the measurement is quite small, indicating high confidence in the result, despite large errors in measurement precision. The maximum anisotropy signature in the data arises under constant stress (Reuss) conditions. Any contribution from constant strain (Voigt) conditions will tend to

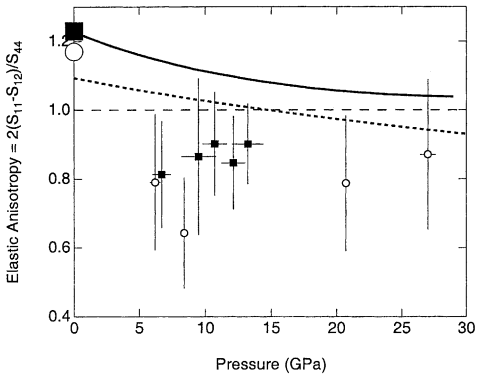

Fig. 5. Plot of elastic anisotropy measured for the hydrous (squares) and anhydrous (open circles) ringwoodite [1] radial diffraction data. Also shown are corresponding ambient pressure values for hydrous ringwoodite (filled square) and anhydrous ringwoodite (open circle) determined by Brillouin spectroscopy [17,19], and high pressure data for anhydrous ringwoodite [20]. The dashed line shows elastic anisotropy calculated by Kiefer et al. [25].

damp out the anisotropy signature – i.e. the slopes of the lines shown in Fig. 3 will become shallower. Therefore the measurement determined here provides a bound on the actual anisotropy; the actual value might be significantly lower than 0.87(7). Eq. 3 shows that the sense of the anisotropy (in this case less than unity) is even more robust, since the anisotropy direction is insensitive to errors in differential stress, pressure, equation of state, and assumption of Reuss conditions.

The most important assumption affecting the interpretation of the lattice anisotropy is that there is no strength anisotropy – that each lattice plane can support the same stress. If this is so (and some alternatives are explored below), the straightforward interpretation of these results is that the high pressure elastic anisotropy of ringwoodite shows a reversal in sense from the ambient measurements [17] and other high pressure measurements [20]. Both of those measurements, which determine the anisotropy of anhydrous ringwoodite to be ~1.2, were obtained using Brillouin scattering techniques. Some possible interpretations for these conflicting results are as follows. (1) Between room pressure and 6.7 GPa the anisotropy decreases and changes signs; (2) lattice plane anisotropy measured in these non-hydrostatic experiments is due to lattice plane-dependent strength effects rather than elastic anisotropy. A third possibility is that the Brillouin scattering experiments are somehow providing an overestimate of the elastic anisotropy. Perhaps there is a frequency dependence to the anisotropy response; therefore high frequency Brillouin experiments are probing a different anisotropy regime than are diamond cell experiments. Seismic frequencies are intermediate between these two regimes.

The decrease and eventual sense reversal of anisotropy observed in these experiments is predicted with first principles calculations of the elastic behavior of ringwoodite under pressure [25] that show anisotropy decreasing with pressure, with a reversal at ~14 GPa. However, alternative methods to induce an apparent lattice strain anisotropy need to be considered to rule out anelastic effects that may arise from point, line, and planar defects. The ringwoodite sample is composed of an aggregate of μm-sized crystallites, approximately randomly oriented. Since each crystallite is in a different orientation with respect to the macroscopic stress state, the critical resolved shear stress (the shear stress required to induce dislocation motion, and therefore plastic deformation, within that grain) will vary from grain to grain [16]. Although the low temperature slip systems for ringwoodite are unknown, the face-centered-cubic (fcc) {111}⟨110⟩ slip system is known for the similarly structured $MgAl_2O_4$ spinel. Because of the high symmetry of the fcc structure, many slip systems are available, and therefore the grain-to-grain ability to support a differential shear stress should not vary widely [16]. This mechanism is testable with our current data. These defects (microstrains) contribute to peak broadening, intensity loss, and preferred orientation, and in addition, may create systematic X-ray diffraction line shifts [26]. Ringwoodite has a structure analogous with $MgAl_2O_4$ spinel, which is based on a fcc lattice. Dislocation slip, twinning, and faulting are primary causes of plastic deformation in these structures [16]. Planar defects such as twinning and faulting in fcc-structured materials create systematic displacements of lattice peaks as well as broadening [26]. A detailed analysis of the magnitude of these shifts, based on analyzing the probability of a twin defect on adjacent planes, and summing the results on average lattice plane spacing in reciprocal space [26] predicts a very different (*hkl*) dependence, with (220) and (400) lines having the maximum positive shift, and the (440) line shift in the

Table 2
Slope and χ^2 values for fits of straight lines shown in Fig. 3a,b

Experiment number	Γ slope	χ^2	Faulting slope	χ^2
1	0.0037	2.40	−2.30E-05	4.68
2	0.0012	2.84	−0.0008	2.86
3	0.0001	2.09	0.0017	0.40
4	0.0006	3.01	0.0008	2.52
5	0.0020	1.12	0.0004	2.31
6	0.0023	3.18	0.0003	5.23
Average	0.0017	2.44	0.0004	3.00

negative direction. The highest pressure data set was analyzed in terms of this faulting probability, yielding a plot similar to Fig. 3a, but with the x-axis tracking peak shifts that would be induced by faulting rather than elastic anisotropy (Fig. 3b). Linear fits to these faulting plots are shown in Fig. 3, and values for the slope and χ^2 are given in Table 2. The fits of the data to the faulting model (Fig. 3b) yield lower slopes (near zero), with slightly worse fits as evidenced by lower χ^2 values than the elastic anisotropy analysis. This result suggests that elastic anisotropy is a better explanation for the observed lattice-dependent response than faulting and twinning.

5. Conclusions

Though these measurements are far from the conditions of the Earth's mantle, especially in temperature, strain rate, and perhaps grain size [27], two important results are raised from these results that have direct implications in interpreting seismic evidence from the Earth's transition zone. First, these strongly bolster the evidence that the presence of OH^- in mantle materials may lead to different rheologic behavior, including less of an ability to support a deviatoric stress; and more deformation (perhaps accompanied by increased lattice preferred orientation, if recrystallization is unperturbed) at a fixed strain rate. This observation may have implications for interpretations of mid-mantle deformation inferred from seismic anisotropy [28]. The second result is that this data set seems to suggest that ringwoodite possesses a larger anisotropy than previously assumed, with a reversed sense. Previously, it had been assumed that anisotropy of ringwoodite within the transition zone was low [29], consistent with Brillouin scattering measurements [20], which show anisotropy gradually decreasing with pressure (Fig. 5). This assumption made it difficult to account for the observed seismic anisotropy, even given the uncertainties in determining how flow geometry and fast directions are correlated [30]. These new radial diffraction results suggest that ringwoodite might have a significant elastic anisotropy within the transition zone, and therefore may help account for the observed mantle seismic anisotropy [11,28].

Acknowledgements

A.K. was supported by a Lamont-Doherty Earth Observatory Postdoctoral Fellowship. Thank you to Joe Smyth for generously supplying the hydrous ringwoodite sample. Research was carried out at the National Synchrotron Light Source, Brookhaven National Laboratory, which is supported by the U.S. Department of Energy, Division of Materials Sciences and Division of Chemical Sciences, under Contract No. DE-AC02-98CH10886. Thanks to Jingzhu Hu at NSLS beamline X17C for experimental assistance. I thank P. Bird, S. King, S. Merkel, and J. Mosenfelder for helpful comments on the manuscript. *[SK]*

References

[1] A. Kavner, T.S. Duffy, Strength and elasticity of ringwoodite at upper mantle pressures, Geophys. Res. Lett. 28 (2001) 2691–2694.
[2] D.R. Bell, G.R. Rossman, Water in earth's mantle: The role of nominally anhydrous minerals, Science 255 (1992) 1391–1397.
[3] J.R. Smyth, β-Mg_2SiO_4 – a potential host for water in the mantle, Am. Mineral. 72 (1987) 1051–1055.
[4] J.W. Downs, Possible sites for protonation in β-Mg_2SiO_4 from an experimentally derived electrostatic potential, Am. Mineral. 74 (1989) 1124–1129.
[5] T.E. Young, H.W. Green, A.M. Hofmeister, D. Walker, Infrared spectroscopic investigation of hydroxyl in β-$(Mg,Fe)_2SiO_4$ and coexisting olivine – implications for mantle evolution and dynamics, Phys. Chem. Mineral. 19 (1993) 409–422.
[6] J.R. Smyth, T. Kawamoto, S.D. Jacobsen, R.J. Swope, R.L. Hervig, J.R. Holloway, Crystal structure of monoclinic hydrous wadsleyite [β-$(Mg,Fe)_2SiO_4$], Am. Mineral. 82 (1997) 270–275.
[7] N. Bolfan-Casanova, H. Keppler, D.C. Rubie, Water partitioning between nominally anhydrous minerals in the MgO-SiO_2-H_2O system up to 24 GPa: Implications for the distribution of water in the Earth's mantle, Earth Planet. Sci. Lett. 182 (2000) 209–221.
[8] J.R. Smyth, C.M. Holl, D.J. Frost, S.D. Jacobsen, F. Langenhorst, C. McCammon, Structural systematics of

hydrous ringwoodite and water in earth's interior, Am. Mineral. 2003 (in press).
[9] G. Hirth, D.L. Kohlstedt, Water in the oceanic upper mantle: Implications for rheology, melt extraction and the evolution of the lithosphere, Earth Planet. Sci. Lett. 144 (1996) 93–108.
[10] G. Nolet, A. Zielhuis, Low s-velocities under the Tornquist-Teisseyre zone – evidence for water injection into the transition zone by subduction, J. Geophys. Res. 99 (1994) 15813–15820.
[11] J. Trampert, H.J. van Heijst, Global azimuthal anisotropy in the transition zone, Science 296 (2002) 1297–1299.
[12] A.K. Singh, The lattice strains in a specimen (cubic system) compressed nonhydrostatically in an opposed anvil device, J. Appl. Phys. 73 (1993) 4278–4286.
[13] A.K. Singh, C. Balasingh, H.-k. Mao, R.J. Hemley, J. Shu, Analysis of lattice strains measured under nonhydrostatic pressure, J. Appl. Phys. 83 (1998) 7567–7575.
[14] T.S. Duffy, G.Y. Shen, D.L. Heinz, J.F. Shu, Y.Z. Ma, H.K. Mao, R.J. Hemley, A.K. Singh, Lattice strains in gold and rhenium under nonhydrostatic compression to 37 GPa, Phys. Rev. B 60 (1999) 15063–15073.
[15] T.S. Duffy, G.Y. Shen, J.F. Shu, H.K. Mao, R.J. Hemley, A.K. Singh, Elasticity, shear strength, and equation of state of molybdenum and gold from x-ray diffraction under nonhydrostatic compression to 24 GPa, J. Appl. Phys. 86 (1999) 6729–6736.
[16] G.E. Dieter, Mechanical Metallurgy, McGraw Hill, New York, 1986, 751 pp.
[17] T. Inoue, D.J. Weidner, P.A. Northrup, J.B. Parise, Elastic properties of hydrous ringwoodite (gamma-phase) in Mg_2SiO_4, Earth Planet. Sci. Lett. 160 (1998) 107–113.
[18] F. Birch, Finite strain isotherm and velocities for single-crystal and polycrystalline NaCl at high pressures and 300 K, J. Geophys. Res. 83 (1978) 1257–1268.
[19] D.J. Weidner, H. Sawamoto, S. Sasaki, M. Kumazawa, Single-crystal elastic properties of the spinel phase of Mg_2SiO_4, J. Geophys. Res. 89 (1984) 7852–7860.
[20] S.V. Sinogeikin, J.D. Bass, T. Katsura, Single-crystal elasticity of γ-$(Mg_{0.91}Fe_{0.09})_2SiO_4$ to high pressures and to high temperatures, Geophys. Res. Lett. 28 (2001) 4335–4338.
[21] G.L. Kinsland, The effect of the strength of materials on the interpretation of data from opposed-anvil high-pressure devices, High Temp. High Press. 10 (1978) 627–639.
[22] C. Meade, R. Jeanloz, Yield strength of MgO to 40 GPa, J. Geophys. Res. 93 (1988) 3261–3269.
[23] C. Meade, R. Jeanloz, Yield strength of the B1 and B2 phases of NaCl, J. Geophys. Res. 93 (1988) 3270–3274.
[24] C. Meade, R. Jeanloz, The strength of mantle silicates at high pressures and room temperature: Implications for the viscosity of the mantle, Nature 348 (1990) 533–535.
[25] B. Kiefer, L. Stixrude, R.M. Wentzcovitch, Calculated elastic constants and anisotropy of Mg_2SiO_4 spinel at high pressure, Geophys. Res. Lett. 24 (1997) 2841–2844.
[26] B.E. Warren, X-ray Diffraction, Addison-Wesley, Reading, MA, 1969, 381 pp.
[27] H.J. Frost, M.F. Ashby, Deformation-Mechanism Maps: The Plasticity and Creep of Metals and Ceramics, Pergamon Press, Oxford, 1982, ix, 166 pp.
[28] J. Wookey, J.M. Kendall, G. Barruol, Mid-mantle deformation inferred from seismic anisotropy, Nature 415 (2002) 777–780.
[29] D. Mainprice, G. Barruol, W. Ben Ismail, The seismic anisotropy of the earth's mantle: From single crystal to polycrystal, in: S. Karato, A. Forte, R. Liebermann, G. Masters, L. Stixrude (Eds.), Earth's Deep Interior: Mineral Physics and Tomography from the Atomic to the Global Scale, AGU Geophys. Monogr. 117 (2000) 237–264.
[30] H. Jung, S. Karato, Water-induced fabric transitions in olivine, Science 293 (2001) 1460–1463.